NOTES AND CORRESPONDENCE

An Analysis of the Nonhydrostatic Dynamics in Numerically Simulated Antarctic Katabatic Flows*

JOHN J. CASSANO AND THOMAS R. PARISH

Department of Atmospheric Science, University of Wyoming, Laramie, Wyoming

23 February 1999 and 14 October 1999

ABSTRACT

A series of two-dimensional numerical experiments was conducted in order to describe the role of nonhydrostatic dynamics in simple Antarctic katabatic flows. The results presented include a comparison of the thermodynamic and dynamic fields produced by hydrostatic and nonhydrostatic numerical simulations. The source of the differences in the simulations was diagnosed based on an analysis of the model equation tendencies as well as calculated components of the pressure gradient force. Over most of the terrain slope, the nonhydrostatic effects were found to be insensitive to the model horizontal resolution, for a grid spacing ranging from 5 to 100 km.

1. Introduction

Antarctic katabatic winds have been studied with both observational data and output derived from numerical simulations (e.g., see Stearns et al. 1993; Parish et al. 1997). Results from numerical simulations of Antarctic katabatic winds have been published in the refereed literature since the early 1980s, starting with Parish (1984). Since this time, there have been many improvements in the numerical models used for these simulations, including enhanced resolution and improved parameterizations of physical processes [see Cassano (1998) for a summary of Antarctic katabatic wind numerical simulations].

One advance that has been lacking in the simulation of Antarctic katabatic flows is the use of numerical models that employ nonhydrostatic governing dynamics, despite the increased use of this model configuration in other areas of atmospheric research. The current note will present the results of idealized two-dimensional (2D) simulations of Antarctic katabatic winds using a nonhydrostatic numerical model. Specifically, the differences in the dynamic and thermodynamic fields in katabatic flows simulated with hydrostatic and nonhydrostatic governing dynamics will be described, and the source of these differences will be explained.

This research was motivated by the increasing number of mesoscale models that use nonhydrostatic dynamics and will serve to document the impact that changing model dynamics from hydrostatic to nonhydrostatic has on simulated katabatic flows, providing a link between previous simulations performed with hydrostatic numerical models and future simulations that will increasingly use nonhydrostatic models. As an example of the current trend toward switching from hydrostatic numerical models to nonhydrostatic numerical models, the most recent version of the Pennsylvania State University–National Center for Atmospheric Research Fifth-Generation Mesoscale Model (MM5 version 3) (released for public use in July 1999) uses nonhydrostatic dynamics only, compared to version 2 of this model, which could employ either hydrostatic or nonhydrostatic dynamics (Dudhia 1999).

In the following sections a brief description of the numerical model that was used will be given, followed by a comparison of the hydrostatic and nonhydrostatic simulations and a more detailed analysis of the source of the nonhydrostatic effects in the simulations. The reader is referred to discussions in Holton (1992) and Bluestein (1993) for a review of the hydrostatic approximation.

2. Model description

The simulations to be presented in this paper were conducted with the MM5 (version 2.9). This model was

* Byrd Polar Research Center Contribution Number 1167.

Corresponding author address: Dr. John J. Cassano, Polar Meteorology Group, Byrd Polar Research Center, The Ohio State University, 1090 Carmack Road, Columbus, OH 43210.
E-mail: cassano@polarmet1.mps.ohio-state.edu

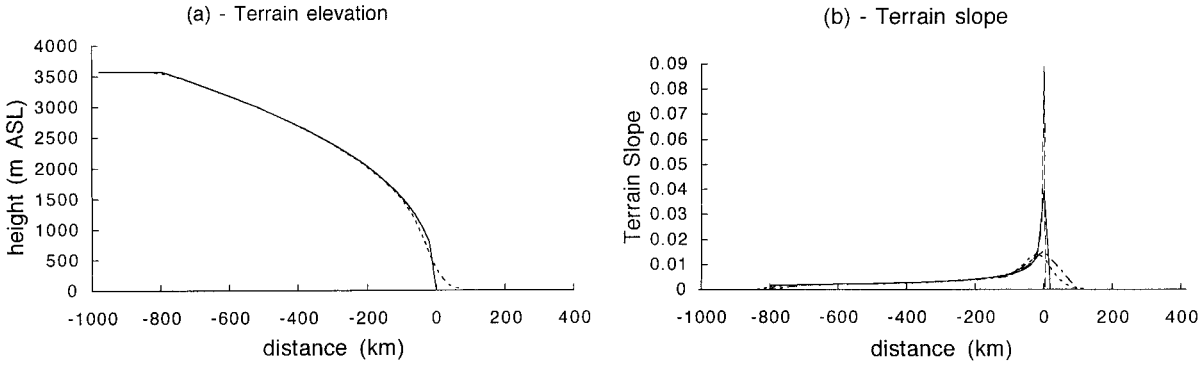

FIG. 1. (a) Terrain elevations given by (1) and used for the 20-km simulations. Solid lines represent the unsmoothed model terrain elevations and the short dashed lines represent the smoothed model terrain elevations. (b) Terrain slopes resolved at 20-km (solid line), 5-km (long dashed line), 100-km (dash dot line), and smoothed 20-km (short dashed line) model horizontal resolutions.

selected for the current project because it provides options for the use of either hydrostatic or nonhydrostatic model dynamics, while allowing the rest of the modeling system to remain unchanged. The MM5 has been described in detail in Dudhia (1993) and Grell et al. (1994).

The simulations were performed with a 2D version of MM5, which was configured for use with dry dynamics only (latent heat fluxes from the surface were neglected as were cloud and precipitation processes). The model physics included a 1.5-order local turbulence closure parameterization (Burk and Thompson 1989), the Zhang and Anthes (1982) surface layer parameterization, and the Community Climate Model 2 radiation parameterization (Hack et al. 1993).

In the horizontal direction the model domain extends from 1000 km inland of the Antarctic coast to 400 km over the adjacent ocean. The oceanic portion of the model domain was treated as ice covered to further simplify the analysis of the simulations. The model terrain that was used for the simulations was derived from a power law fit to the ice topography along the 90°E meridian of Antarctica, given by Parish and Waight (1987), and takes the form

$$
\begin{aligned}
z_g &= z_g(x = -800 \text{ km}), \quad \text{for } x < -800 \text{ km} \\
z_g &= 3922.2\left(1 - \frac{1000 \text{ km} + x}{1000 \text{ km}}\right)^{0.4112}, \\
&\qquad \text{for } -800 \text{ km} \le x \le 0 \text{ km} \\
z_g &= 0, \qquad \text{for } x > 0 \text{ km}, \qquad (1)
\end{aligned}
$$

where z_g is the terrain elevation in meters and x is the distance from the Antarctic coastline, with negative distances over the continent and positive distances over the ocean. The terrain heights given by (1) are shown in Fig. 1a. The slope of the model terrain, as resolved at various model horizontal resolutions, is plotted in Fig. 1b.

In the vertical direction, a sigma-level terrain-following coordinate system was used, with 25 levels in the vertical that extended from the surface to a pressure of 25 000 Pa at the model top. The lowest sigma level was located at a nominal height of 14 m above ground level (AGL), and seven sigma levels were located within 210 m of the surface to more accurately represent the processes occurring in the katabatic layer. The spacing of the vertical levels was uneven and a geometric stretching, with a factor of 1.2, was applied to the distance between adjacent levels.

All of the simulations that will be presented in this paper were initialized with no horizontal temperature or pressure gradient, and a constant temperature lapse rate from the surface to the model top. The temperature profile is similar to that given by Schwerdtfeger (1984, their Fig. 6.9) for Byrd Station, Antarctica, and is representative of conditions prior to the onset of rapid surface cooling during the austral winter. The effects of solar radiation are not considered in this work, also making the simulations representative of austral winter conditions. Simulations in which a constant background horizontal pressure gradient was specified produced qualitatively similar results to those with zero ambient pressure gradient and, in the interest of space, will not be presented.

3. Comparison of hydrostatic and nonhydrostatic simulations

A series of numerical experiments was conducted in which the horizontal grid spacing was varied from 5 to 100 km. These simulations produced dynamic and thermodynamic fields that were quite similar. The largest differences in these simulations occurred near the coastline, where the downslope wind speed increased with increases in the horizontal grid distance. This somewhat surprising result, given the shallower terrain slopes represented in the coarser-resolution simulations (Fig. 1b), was the result of changes in the depth and intensity of a cold pool of air that accumulated just offshore of the continent and acted to retard the coastal winds. As will be shown below, this effect is a purely hydrostatic consideration and thus not of interest in this paper. The

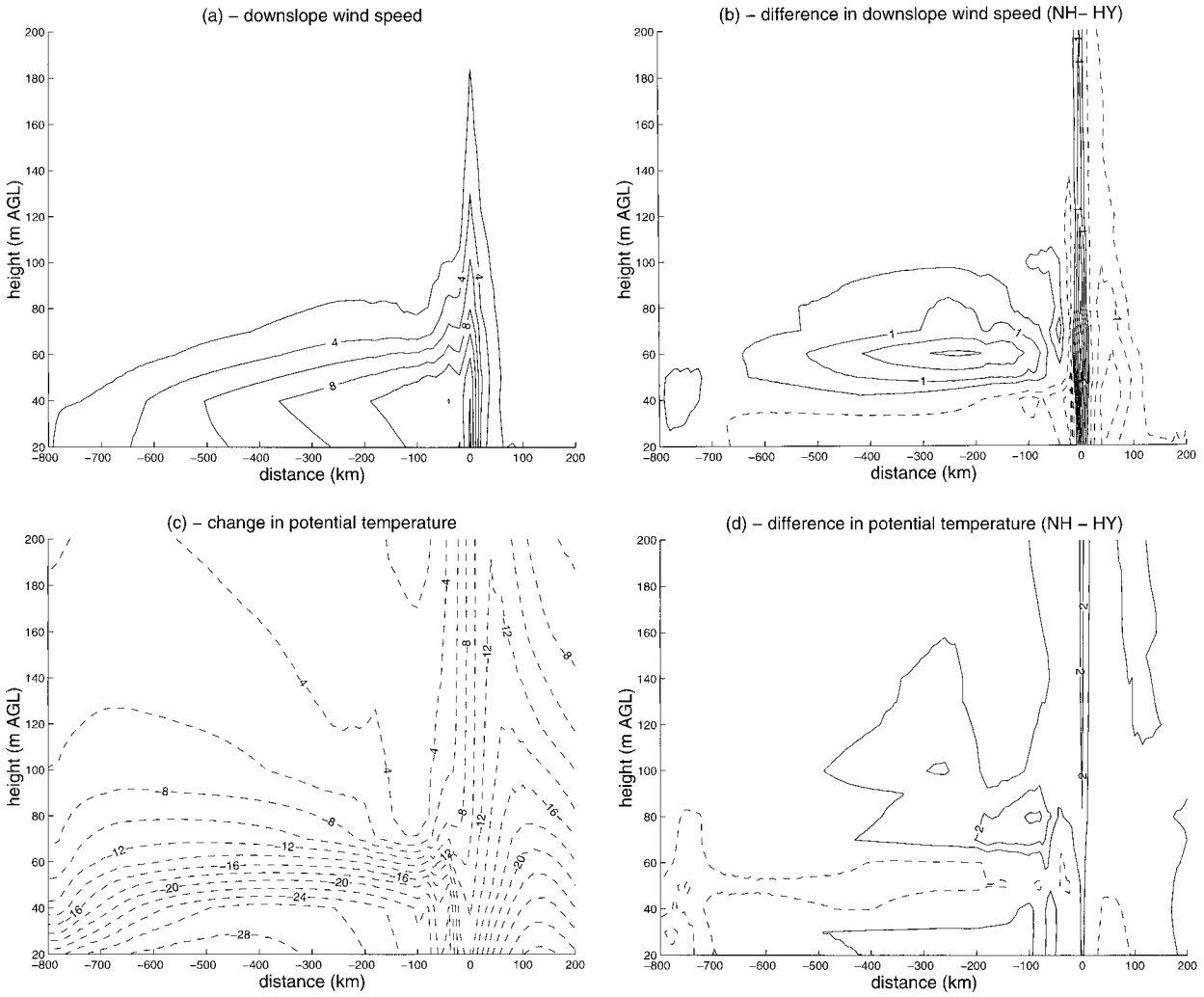

FIG. 2. Cross sections of the (a) downslope wind speed and (c) change in potential temperature for the 20-km nonhydrostatic simulation, and the differences in the (b) downslope wind speed and (d) potential temperature between the nonhydrostatic (NH) and hydrostatic (HY) 20-km simulations (NH − HY) after 24 h of model integration. Solid contours represent positive values, dashed contours represent negative values, and the zero contour has been omitted. The contour interval is 2 m s^{-1} for (a), 0.5 m s^{-1} for (b), 2 K for (c), and 1 K for (d). Note that the vertical axis is given as height AGL rather than height above mean sea level.

nonhydrostatic effects, which were found to be largest inland of the coast, are quantitatively similar for all of the horizontal grid spacing experiments considered. Therefore, results from the 20-km horizontal-grid spacing experiment will be the focus of this paper. Figure 2 shows cross sections of the downslope wind speed and change in potential temperature for the nonhydrostatic simulation after 24 h of model integration as well as the difference of these fields between the nonhydrostatic and hydrostatic simulations.

The downslope wind speed was found to be more than 0.5 m s^{-1} weaker for the nonhydrostatic simulation compared to the hydrostatic simulation, below 40 m AGL over much of the terrain slope (Fig. 2b). In addition the downslope flow was up to 2 m s^{-1} stronger above this level in the nonhydrostatic simulation. Large differences in the wind speed were also present along the coastline and over the adjacent ocean, where differences as large as 3 m s^{-1} occurred.

The thermodynamic fields also differed between the hydrostatic and nonhydrostatic simulations (Fig. 2d). Over much of the terrain slope, the hydrostatic simulation was found to be cooler than the nonhydrostatic simulation, with differences as large as 2 K. Over the adjacent ocean, the nonhydrostatic simulation was cooler within approximately 100 km of the coastline, again with differences as large as 2 K.

Aside from documenting the differences in the thermodynamic and dynamic fields simulated with the hydrostatic and nonhydrostatic versions of the model, an understanding of the source of these differences was sought. The generally cooler atmosphere over the continental portion of the model domain in the hydrostatic simulations was found to be caused by a larger down-

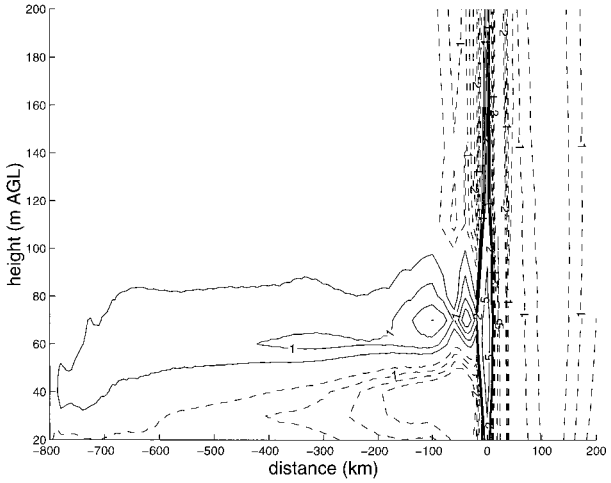

FIG. 3. As in Fig. 2 except that the difference in the downslope PGF between the nonhydrostatic (NH) and hydrostatic (HY) 20-km simulations (NH − HY) after 24 h of model integration is plotted. The contour interval is 0.5 m s^{-1} h^{-1} for contour magnitudes less than or equal to 2 m s^{-1} h^{-1}, and 5 m s^{-1} h^{-1} for contour magnitudes greater than or equal to 5 m s^{-1} h^{-1}.

ward directed sensible heat flux, from the atmosphere to the surface. This larger sensible heat flux was forecast by the surface layer parameterization in response to the stronger flow at the lowest model level in the hydrostatic simulation (which, as will be shown below, was a direct result of the nonhydrostatic dynamics). Differences in the downslope flow, between the hydrostatic and nonhydrostatic simulations, are intimately tied to differences in the downslope pressure gradient force (PGF) forecast by the model. The source of the differences in the downslope PGF in the simulations, and thus the source of the differences in the downslope flow, will be discussed below.

Figure 3 shows a cross section of the difference in the forecast downslope PGF after 24 h of model integration (note that the PGF plotted in this figure was output directly from the numerical model rather than being calculated based on the standard model output of the thermodynamic fields). The nonhydrostatic simulation has a weaker downslope PGF below 40 m AGL over much of the terrain slope and a stronger downslope PGF above this level. Differences in the downslope PGF over the continent are as large as 2 m s^{-1} h^{-1}, with maxima in this difference field located 40 to 100 km inland from the coast. Additional differences are also present near the coast and over the adjacent ocean. The downslope PGF is up to 5 m s^{-1} h^{-1} stronger at the coast and 1.5 m s^{-1} h^{-1} weaker over the oceanic portion of the model domain, in the nonhydrostatic simulation.

In order to understand the source of the differences in the downslope PGF forecast by the nonhydrostatic and hydrostatic versions of the model, an analysis based on the classic equations used to describe slope flows was performed. These classic slope-flow equations relate changes in cooling along and normal to the terrain slope to specific components of the downslope PGF. Following Mahrt (1982) the total downslope PGF can be represented as

$$\mathrm{PGF} = g\frac{d}{\theta_0}\sin\alpha - \cos\alpha\frac{g}{\theta_0}\frac{\partial\overline{\overline{d}}}{\partial x} - \frac{1}{\rho}\frac{\partial p}{\partial x}\bigg|_{\mathrm{back}}. \quad (2)$$

Reading from left to right, on the rhs of (2), the three terms are referred to as the buoyancy, adverse PGF, and background PGF terms, respectively. The variables represented in (2) include the potential-temperature deficit, d; the reference potential temperature, θ_0; and the terrain slope, α. Other more commonly used variables include g, ρ, p, and x, which represent the acceleration due to gravity, the density of air, the total pressure, and the horizontal coordinate, which is parallel to the terrain slope, respectively. The double overbar, in the second term on the rhs of (2), is used to denote a vertical average over the depth of the cooled layer. The three terms on the rhs of (2) were evaluated using the model output thermodynamic fields and PGF (for the background PGF term). The background PGF term was taken as the model-calculated PGF at the top of the katabatic layer.

In this analysis it is possible to isolate differences in the downslope PGF between the hydrostatic and nonhydrostatic simulations that are caused by differences in the forecast temperature fields. These differences arise from purely hydrostatic considerations, since (2) is derived for hydrostatically balanced flows (Mahrt 1982). It should be noted that (2) cannot account for any component of the PGF that arises through nonhydrostatic considerations (i.e., a pressure distribution that is not in hydrostatic balance with the forecast temperature field), and this fact will be used in the determination of the nonhydrostatic component of the PGF in the next section of this paper.

Comparison of the PGF terms calculated with (2) from the hydrostatic and nonhydrostatic model output revealed that the background PGF term was nearly identical for both simulations. In contrast, both the buoyancy and adverse PGF terms differed between the hydrostatic and nonhydrostatic simulations. These differences in the buoyancy and adverse PGF terms were caused by differences in the simulated thermodynamic fields in the two simulations. The large differences in the model-predicted downslope PGF at the coast and over the oceanic portion of the model domain (Fig. 3) were attributable to differences in the buoyancy and adverse PGF terms (and thus differences in the temperature distribution) and were not a direct result of differences between the hydrostatic and nonhydrostatic dynamics (the nonhydrostatic component of the PGF discussed below). The difference in the downslope PGF between the hydrostatic and nonhydrostatic simulations inland of the coast (Fig. 3) could not be attributed to differences in the hydrostatic components of the PGF [as calculated with (2)]. In the following section an analysis of the nonhydrostatic dynamics and the source of the differ-

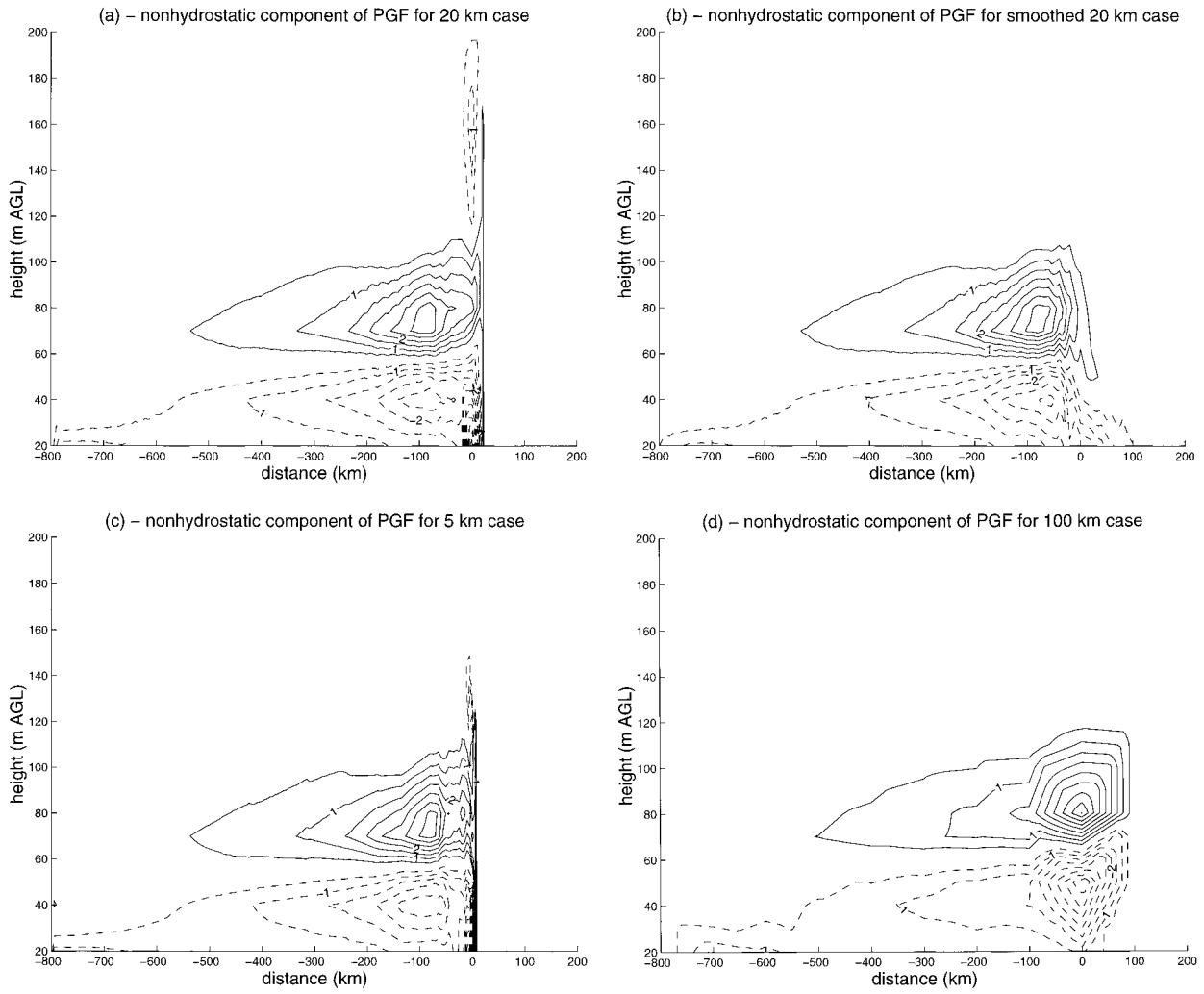

FIG. 4. As in Fig. 2 except that the calculated nonhydrostatic component of the PGF for the (a) 20-km, (b) smoothed-terrain 20-km, (c) 5-km, and (d) 100-km nonhydrostatic simulations after 24 h of model integration are plotted. The contour interval is 0.5 m s^{-1} h^{-1} for (a)–(d).

ences in the simulated downslope PGF over the continent will be presented.

4. Analysis of the nonhydrostatic dynamics

Calculating the PGF with the classic (hydrostatic) slope-flow equation (2) when the flow is governed by nonhydrostatic dynamics will result in the calculated downslope PGF (PGF_{calc}) not being equal to the numerical model predicted downslope PGF (PGF_{model}). The difference between PGF_{calc} and PGF_{model} is a measure of the component of the PGF due to nonhydrostatic effects (PGF_{NH}). This can be shown as

$$PGF_{NH} = PGF_{model} - PGF_{calc}. \quad (3)$$

This relationship has been verified by evaluating PGF_{NH} for the hydrostatic simulations, which should be equal to zero. In this analysis the magnitude of PGF_{NH} was less than 0.1 m s^{-1} h^{-1} over the terrain slope, with slightly larger differences present at the coast. In contrast, PGF_{NH} is of much larger magnitude when calculated from output taken from the nonhydrostatic simulation and is organized in a coherent fashion consistent with the differences in the model-predicted PGF for the nonhydrostatic and hydrostatic simulations (Fig. 3).

A cross section of the calculated nonhydrostatic PGF for the 20-km, nonhydrostatic simulation is shown in Fig. 4. In addition, the nonhydrostatic PGF for the nonhydrostatic 5- and 100-km simulations are also shown in this figure. Consistent with the discussion in section 3, the nonhydrostatic component of the PGF over much of the terrain slope is nearly identical for the range of horizontal resolutions considered in this series of numerical experiments. Differences in the nonhydrostatic

PGF for these simulations are present within 20 km of the coast, particularly at lower levels. These differences are caused by the steeper representation of the model terrain with increasing horizontal resolution (Fig. 1b). Farther inland the nonhydrostatic PGF is quite similar for all three simulations. This lack of sensitivity to model horizontal resolution is caused by the nearly identical representation of the model terrain at these resolutions (Fig. 1b). The nonhydrostatic component of the PGF (Fig. 4a) largely explains the difference in the model-forecast PGF between the nonhydrostatic and hydrostatic simulations over the continent (Fig. 3), with slight differences attributable to modulation by the buoyancy and adverse PGF components.

The role of the singularity in the model terrain at the coast ($x = 0$ km; Fig. 1a) was addressed in an additional numerical experiment in which five passes of a smoother–desmoother filter (Grell et al. 1994) were applied to the terrain given by (1). This smoothed terrain is shown in Fig. 1a as a short dashed line and $\mathrm{PGF}_{\mathrm{NH}}$ calculated from the model output for this simulation is shown in Fig. 4b. The $\mathrm{PGF}_{\mathrm{NH}}$ inland of $x = -50$ km is nearly identical for the original 20-km horizontal-resolution simulation (Fig. 4a) and the simulation that used the smoothed terrain (Fig. 4b). Based on this numerical experiment, it appears that the singularity in the model terrain generates a nonhydrostatic response locally and that the nonhydrostatic component of the PGF over the rest of the terrain slope is a response to the larger-scale topographic forcing.

Numerical experiments using model terrain given by an inclined plane (constant slope) resulted in a nonhydrostatic component of the PGF that was qualitatively similar to that found for the Antarctic terrain experiments (i.e., negative $\mathrm{PGF}_{\mathrm{NH}}$ at low levels and positive $\mathrm{PGF}_{\mathrm{NH}}$ at upper levels). In these experiments the terrain slope was varied from 0.000 25 to 0.006 (similar to the Antarctic model terrain slopes between $x = -500$ km and $x = -100$ km). The magnitude of $\mathrm{PGF}_{\mathrm{NH}}$ increased as the terrain slope increased (and the intensity of the katabatic flow increased) and had a magnitude similar to that found in the Antarctic terrain experiments. Based on these experiments, it was concluded that the nonhydrostatic effects discussed in this paper will be present in katabatic flows over a variety of sloped surfaces (from simple inclined planes to concave terrain profiles) and will increase in magnitude as the terrain slope increases.

Differences in the dynamic and thermodynamic fields observed in the hydrostatic and nonhydrostatic Antarctic katabatic wind numerical simulations have been described along with the forcing for these differences. The weaker flow at low levels in the katabatic layer, in the nonhydrostatic simulation, is due to a nonhydrostatically driven component of the PGF that opposes the downslope acceleration of the air. Conversely, the enhanced drainage flow aloft in the nonhydrostatic simulation is the result of a downslope directed nonhydrostatic component of the PGF. One final issue that requires attention concerns the forcing for the nonhydrostatic PGF. In order to address this problem, terms from the MM5 pressure tendency equation were output for further analysis.

The perturbation pressure tendency equation from MM5 is given by

$$\frac{\partial p^* p'}{\partial t} = -\frac{\partial p^* u p'}{\partial x} - \frac{\partial p^* p' \dot{\sigma}}{\partial \sigma} + p' \,\mathrm{DIV} - p^* \gamma p \left[\frac{\partial u}{\partial x} - \frac{\sigma}{p^*}\frac{\partial p^*}{\partial x}\frac{\partial u}{\partial \sigma}\right] + \rho_0 g \gamma p \frac{\partial \omega}{\partial \sigma} + p^* \rho_0 g \omega. \quad (4)$$

The variables in this equation include the perturbation pressure p', the surface pressure minus the pressure at the model top p^*, time t, the downslope wind speed u, the vertical velocity in the sigma coordinate system $\dot{\sigma}$, the pressure vertical velocity ω, the horizontal coordinate x, the vertical coordinate σ, a mass divergence term DIV (which is related to the advective terms), the ratio of the heat capacity of dry air at constant pressure to that at constant volume γ, reference density ρ_0, and the acceleration due to gravity g. The sum of the first three terms on the rhs of (4) represents the advection of the perturbation pressure; the fourth term represents the effects due to convergence of the horizontal component of the wind; the fifth term represents the effects due to convergence of the vertical component of the wind; and the last term represents the vertical advection of the reference state pressure. In the discussion that follows, the first three terms on the rhs of (4) have been combined with the last term on the rhs of (4) to give the total advective tendency, while the horizontal and vertical convergence terms have been combined to give the total convergence term.

Cross sections of the pressure tendency terms, 24 h after the start of the model integration, are shown in Fig. 5. Based on a time series analysis of these terms, the cross sections are representative of the forcing for the perturbation pressure tendency for the duration of the model integration. The advection and total convergence terms are of equal magnitude and opposite sign and they nearly balance, causing the total perturbation pressure tendency to be two orders of magnitude smaller than either the advection or convergence terms. (Note that the calculation of the p' tendency could be subjected to truncation errors since it is calculated as the sum of two large terms of opposite sign, but this is not the same as the truncation error frequently discussed in relation to the calculation of the horizontal PGF over steep terrain slopes in sigma vertical coordinate models.)

The spatial distribution of the pressure tendency needed to generate the nonhydrostatic PGF shown in Fig. 4 requires enhanced pressure rises near the coast, below 60 m AGL, relative to locations farther inland, while above 60 m AGL there must be enhanced pressure falls near the coast relative to locations farther inland. Based

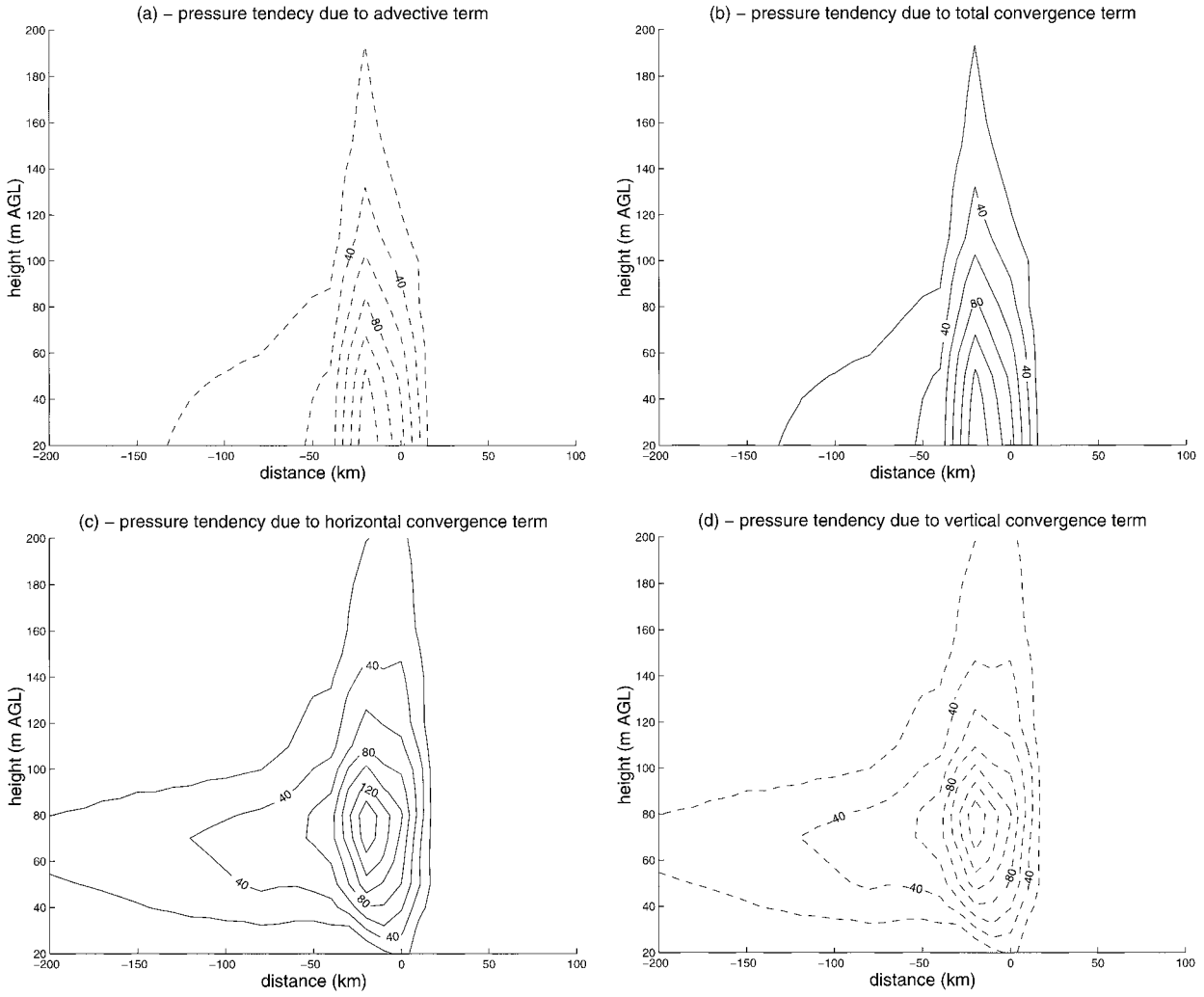

FIG. 5. As in Fig. 2 except that the perturbation pressure tendency due to (a) advection, (b) total convergence, (c) horizontal convergence, and (d) vertical convergence for the 20-km nonhydrostatic simulation after 24 h of model integration are plotted. The contour interval is 2000 Pa h^{-1} for (a) and (b) and 2×10^6 Pa h^{-1} for (c) and (d). The contour values are multiplied by 10^{-2} in (a) and (b) and 10^{-4} in (c) and (d).

on Fig. 5, it is found that the perturbation pressure tendencies consistent with this discussion are caused by the total convergence term at lower levels (Fig. 5b) and by the vertical convergence term at upper levels (Fig. 5d). The advective tendency is not a factor in the generation of the nonhydrostatic PGF shown in Fig. 4.

The physical processes responsible for the various components of the pressure tendency can be understood by considering the horizontal flow field shown in Fig. 2a. The maximum in the horizontal convergence term near the coast (Fig. 5c) is caused by enhanced horizontal convergence near the coast due to the rapid deceleration of the flow over the ocean. In addition this term is increased in response to horizontal convergence of the katabatic flow with the nearly stationary air mass outside of the drainage flow layer (above and away from the terrain), as the terrain slope rapidly falls away just inland of the coast. The vertical motion, and thus the vertical convergence term, can be deduced from the horizontal flow field since the vertical component of the wind is approximately given by the product of the downslope wind speed and the terrain slope. The maximum downward vertical motion at a given distance inland from the coast is collocated with the maximum downslope wind speed. Below the level of maximum downward vertical motion, vertical convergence occurs (forcing pressure rises), while above this level vertical divergence occurs (forcing pressure falls). The greatest vertical divergence occurs near the coast (Fig. 5d) where the downslope flow is strongest, the terrain slope is steepest, and thus the vertical gradient in the vertical motion is largest. Through the horizontal and vertical flow fields, the pressure distribution is modified and gives rise to the nonhydrostatic effects discussed in this paper.

5. Conclusions

This paper represents the first exploration of nonhydrostatic effects acting in numerically simulated Antarctic katabatic winds. As such, the purpose of this paper was to describe the response of simulated katabatic flows to the use of nonhydrostatic governing dynamics in terms of the thermodynamic and dynamic fields that were simulated and to address the forcing mechanisms for the observed differences between the hydrostatic and nonhydrostatic simulations.

The flow was found to be weaker at lower levels and stronger at upper levels in the katabatic layer, when nonhydrostatic, rather than hydrostatic, governing dynamics were employed in the model. The difference in the flow at lower levels led to reduced turbulent sensible heat loss to the surface in the nonhydrostatic simulation, compared to the hydrostatic simulation, and to a generally warmer atmosphere being forecast in the nonhydrostatic simulation. The forcing for the observed differences in the flow was determined through an analysis of the model-forecast PGF as well as diagnosed components of the PGF. This analysis allowed the forcing for the nonhydrostatic effects to be easily interpreted in terms of the physical processes acting in the katabatic flow.

Numerical experiments in which the model terrain was given as an inclined plane generated a nonhydrostatic response that was similar to that found for the Antarctic model terrain. Based on these results it is expected that nonhydrostatic effects will be present in numerical simulations of katabatic winds over a variety of terrain slopes, including the steep coastal margins of the Antarctic and Greenland ice sheets. Future work should address nonhydrostatic effects for more complex terrain configurations as well as for situations with realistic ambient forcing.

Acknowledgments. Thanks must be given to the scientists at the Mesoscale and Microscale Meteorology Division at NCAR for their support and assistance with the use of MM5, to three anonymous reviewers whose comments helped improve this manuscript, and to D. H. Bromwich for his comments on an early version of this manuscript. This research was funded in part by National Science Foundation Grant OPP-9725263 to T. R. Parish.

REFERENCES

Bluestein, H. B., 1993: *Observations and Theory of Weather Systems. Synoptic–Dynamic Meteorology in Midlatitudes.* Vol. II. Oxford University Press, 594 pp.

Burk, S. D., and W. T. Thompson, 1989: A vertically nested regional numerical weather prediction model with second-order closure physics. *Mon. Wea. Rev.,* **117,** 2305–2324.

Cassano, J. J., 1998: The impact of numerical model configuration on simulated Antarctic katabatic winds. Ph.D. dissertation, University of Wyoming, 216 pp. [Available from UMI Dissertation Services, 300 N. Zeeb Rd., P.O. Box 1346, Ann Arbor, MI 48106.]

Dudhia, J., 1993: A nonhydrostatic version of the Penn State–NCAR Mesoscale Model: Validation tests and simulation of an Atlantic cyclone and cold front. *Mon. Wea. Rev.,* **121,** 1493–1513.

——, 1999: Recent development in MM5. Preprints, *Ninth PSU/NCAR Mesoscale Model Users' Workshop,* Boulder, CO, National Center for Atmospheric Research, 3–5.

Grell, G. A., J. Dudhia, and D. R. Stauffer, 1994: A description of the fifth-generation Penn State/NCAR Mesoscale Model (MM5). NCAR Tech. Note NCAR/TN-398+STR, 122 pp.

Hack, J. J., B. A. Boville, B. P. Briegleb, J. T. Kiehl, P. J. Rasch, and D. L. Williamson, 1993: Description of the NCAR Community Climate Model (CCM2). NCAR Tech. Note NCAR/TN-382+STR, 108, pp.

Holton, J. R., 1992: *An Introduction to Dynamic Meteorology.* Academic Press, 511 pp.

Mahrt, L., 1982: Momentum balance of gravity flows. *J. Atmos. Sci.,* **39,** 2701–2711.

Parish, T. R., 1984: A numerical study of strong katabatic winds over Antarctica. *Mon. Wea. Rev.,* **112,** 545–554.

——, and K. T. Waight, 1987: The forcing of Antarctic katabatic winds. *Mon. Wea. Rev.,* **115,** 2214–2226.

——, Y. Wang, and D. H. Bromwich, 1997: Forcing of the austral autumn surface pressure change over the Antarctic continent. *J. Atmos. Sci.,* **54,** 1410–1422.

Schwerdtfeger, W., 1984: *Weather and Climate of the Antarctic.* Elsevier, 261 pp.

Stearns, C. R., L. M. Keller, G. A. Weidner, and M. Sievers, 1993: Monthly mean climatic data for Antarctic automatic weather stations. *Antarctic Meteorology and Climatology: Studies Based on Automatic Weather Stations,* D. H. Bromwich and C.R. Stearns, Eds., Amer. Geophys. Union, 1–21.

Zhang, D., and R. A. Anthes, 1982: A high-resolution model of the planetary boundary layer—Sensitivity tests and comparisons with SESAME-79 data. *J. Appl. Meteor.,* **21,** 1594–1609.